

Type-II Dirac Photons

Hai-Xiao Wang,^{1,*} Yige Chen,^{2,*} Zhi Hong
Hang,¹ Hae-Young Kee,^{2,3,†} and Jian-Hua Jiang^{1,‡}

¹*College of Physics, Optoelectronics and Energy,
& Collaborative Innovation Center of Suzhou Nano Science and Technology,
Soochow University, 1 Shizi Street, Suzhou 215006, China*

²*Department of Physics, University of Toronto, Toronto, M5S 1A7, Canada*

³*Canadian Institute for Advanced Research,
Toronto, Ontario, M5G 1Z8, Canada*

(Dated: November 27, 2017)

* These authors contributed equally.

† hykee@physics.utoronto.ca

‡ jianhua.jiang@suda.edu.cn

Abstract

The Dirac equation for relativistic electron waves is the parent model for Weyl and Majorana fermions as well as topological insulators. Simulation of Dirac physics in three-dimensional photonic crystals, though fundamentally important for topological phenomena at optical frequencies, encounters the challenge of synthesis of both Kramers double degeneracy and parity inversion. Here we show how type-II Dirac points—exotic Dirac relativistic waves yet to be discovered—are robustly realized through the nonsymmorphic screw symmetry. The emergent type-II Dirac points carry nontrivial topology and are the mother states of type-II Weyl points. The proposed all-dielectric architecture enables robust cavity states at photonic-crystal—air interfaces and anomalous refraction, with very low energy dissipation.

Introduction

Dirac’s famous equation for relativistic electron waves [1] is the foundation for both the quantum field theory and the later topological insulators and semimetals [2–4]. There has been a trend in the simulation of relativistic waves and topological states in classical dynamics such as electromagnetic [5, 6], acoustic [7–9] and mechanical waves [10, 11], mostly in 2D systems. Many novel phenomena in electromagnetism are discovered along this paradigm, such as photonic *Zitterbewegung* [12], zero-index dielectric metamaterials [13], deformation induced pseudomagnetic field for photons [14], as well as photonic topological insulators with [15–19] and without [5, 20–24] time-reversal (\mathcal{T}) symmetry. Recently, such simulation develops from 2D to 3D [25–32], exposing to larger wavevector and configuration space that may lead to richer physical phenomena, particularly using \mathcal{T} -invariant materials which are more feasible for high-frequency (e.g., infrared or visible) applications.

Due to its bosonic nature, i.e., $\mathcal{T}^2 = 1$, the four-fold degenerate photonic Dirac points (DPs) can be created only when Kramers double degeneracy (“spin”) and parity-inversion (“orbit”) are *synthesized*. These two elements are also at the heart of Z_2 topology in \mathcal{PT} -symmetric (\mathcal{P} is inversion) systems, as revealed in the seminal work of Fu and Kane [33]. Although there have been a few fine designs [29, 31, 32] showing the connection between type-I DPs and the Z_2 topology, type-II DPs [in analog of type-II Weyl Points (WPs) [34, 35], see Fig. 1] have never been explored in photonics or in other classical/bosonic waves. In

this work, we demonstrate the creation and destruction of type-II DPs in PhCs. Besides, we unveil screw symmetry, a fundamental type of nonsymmorphic symmetry, as an effective tool for the creation of DPs.

The distinction between symmorphic (e.g., point-group) and nonsymmorphic spatial symmetries in crystals lies in whether the spatial origin can be preserved. Nonsymmorphic symmetries cannot preserve the spatial origin but translate it by a fraction of the crystal period. The screw symmetry, a rotation accompanied with a fraction of lattice translation, is an elementary nonsymmorphic symmetry. So far, the role of screw symmetry on the realization of topological states in classical/bosonic waves has not yet been explored. It is known that screw symmetries lead to double degeneracy for all Bloch states on certain planes in the Brillouin zone (BZ) [36, 37]. Thus the screw symmetries can create a large wavevector space for the simulation of DPs and Z_2 topology in classical dynamics. The screw symmetries become particularly powerful when there are two orthogonal screw axes, since the product of the two screw rotations is essentially the parity required by the DPs. In this way both the “Kramers” double degeneracy (“spin”) and parity-inversion (“orbit”) can be simultaneously synthesized through screw symmetry.

Based on these symmetry considerations we propose an all-dielectric tetragonal PhC with screw symmetries for the creation of both type-II and type-I DPs. Our symmetry-guided approach is robust: DPs emerge for a variety of geometry and materials. We demonstrate the nontrivial topology of the DPs by studying the edge states. These non-chiral edge states, differing from the chiral edge states of Weyl points (WPs), are below the light-line and form resilient cavity states on PhC-air interfaces. Moreover, we show that both type-II and type-I WPs can be derived from these DPs when symmetry is reduced. Anomalous refraction with one or two pairs of opposite refraction angles is predicted for type-II DPs/WPs. To the best of our knowledge, this is the discovery of type-II DPs in photonics and a proposal of type-II WPs in *all-dielectric* PhCs. Our findings may enable unprecedented control of light at optical frequencies using dissipationless materials.

Results

All-dielectric photonic-crystal architecture

We study an all-dielectric PhC with tetragonal symmetry of space group $P4_2/mcm$ (see Fig. 2) to illustrate the symmetry-guided approach. In each unit cell, there are two dielec-

tric blocks (painted as yellow and green in Fig. 2) of the same shape and permittivity ε_b , embedded in a polymer matrix of permittivity $\varepsilon_m = 1.9$. We shall first set $\varepsilon_b = 16$ and the geometry parameters $l = 0.5$, $w = 0.2$, and $h = 0.5$ (lattice constant $a \equiv 1$). We show later that DPs emerge for other material/geometric parameters as well. These PhCs can in principle be fabricated using layer-by-layer methods with the current technology [38, 39] for infrared frequencies. We use the MIT PHOTONIC BANDS [40] to calculate the bulk and surface photonic bands. The tetragonal symmetries crucial to our study are the two-fold screw symmetries $S_x := (x, y, z) \rightarrow (\frac{1}{2}+x, \frac{1}{2}-y, \frac{1}{2}-z)$ and $S_y := (x, y, z) \rightarrow (\frac{1}{2}-x, \frac{1}{2}+y, \frac{1}{2}-z)$ (illustrated in Fig. 2b), and the 180° rotation around the z axis, $C_2 := (x, y) \rightarrow (-x, -y)$. The remaining symmetries are listed and analyzed in the Supplementary Materials.

Photonic Kramers double degeneracy

Anti-unitary operators: $\Theta_i \equiv S_i * \mathcal{T}$ ($i = x, y$) are created to elucidate the power of the screw symmetry. The effect of the time-reversal operation \mathcal{T} on a photonic Bloch wavefunction $\Psi_{n\vec{k}}(\vec{r}) = (\vec{e}_{n\vec{k}}, \vec{h}_{n\vec{k}})^T$ is mostly complex conjugation, $\mathcal{T}(\vec{e}_{n\vec{k}}, \vec{h}_{n\vec{k}})^T = (\vec{e}_{n\vec{k}}^*, -\vec{h}_{n\vec{k}}^*)^T$. Since $\Theta_x^2 = S_x^2 = T_{100}$ where T_{100} is a spatial translation by the vector $(1, 0, 0)$, acting Θ_x twice on a photonic Bloch state gives $\Theta_x^2 \Psi_{n\vec{k}}(\vec{r}) = e^{ik_x} \Psi_{n\vec{k}}(\vec{r})$ (see details in Methods). Θ_x transforms (k_x, k_y, k_z) into $(-k_x, k_y, k_z)$ and is hence invariant on the $k_x = \pi$ plane, where we find

$$\Theta_x^2 = e^{ik_x} \Big|_{k_x=\pi} = -1. \quad (1)$$

The above equation, as an analog of the Kramers theorem for fermions, guarantees that *all* photonic states on the $k_x = \pi$ plane are doubly degenerate (see Fig. 2c). Similarly, all Bloch states are doubly degenerate on the $k_y = \pi$ plane due to $\Theta_y^2 = -1$.

Dirac Points

For the creation of DPs, the next important step is to realize parity-inversion. Here the parity is defined through C_2 , which is invariant on the MA line, $k_x = k_y = \pi$. The product of the two orthogonal screw rotations yields, $S_y S_x = T_{010} C_2$ and $S_x S_y = T_{100} C_2$. On the MA line one hence has

$$\Theta_y \Theta_x = \Theta_x \Theta_y = -C_2. \quad (2)$$

Elegantly, the above algebra reveal that the two degenerate states in any doublet have the

same eigenvalue of the C_2 rotation. Such eigenvalues $c_2 = \pm 1$ precisely represent the parities of the photonic states in the x - y plane.

It has been shown in Ref. [29] that a DP with synthetic Kramers double degeneracy and parity-inversion has nontrivial topological properties. In fact, such DPs are monopoles of the $SU(2)$ Berry-phase gauge fields [29]. The topological charge of a DP is defined by the integral of the $SU(2)$ gauge fields over a tiny sphere containing the DP. It was proved in Ref. [41] that in systems with \mathcal{PT} symmetry, the calculation of the topological charge of a DP can be simplified as

$$N_{DP} = \frac{1}{2} [c_2^-(k_0^+) - c_2^-(k_0^-)], \quad (3)$$

where c_2^- is the parity of the lower branch of the Dirac cone, and $k_0^+ = k_0 + 0^+$ ($k_0^- = k_0 - 0^+$) is the wavevector slightly larger (smaller) than that of the DP on the z direction, k_0 . Since the total topological charge of photonic bands in the BZ is strictly zero, DPs emerge in pairs with opposite N_{DP} at opposite wavevectors. Fig. 2d shows that there are four DPs in the first six bands, due to the crossing between the p - and d -doublets.

Our symmetry-guided paradigm provides a robust and effective approach toward topological DPs: Fig. 2e shows that the emergence of DPs is quite robust to the shape and permittivity of the dielectric blocks (more examples are given in the Supplementary Materials), since any crossing between bands of different parities on the MA line leads to DPs.

The spin-orbit physics of the Dirac points can be understood via a symmetry-based $\vec{k} \cdot \vec{P}$ theory (see Supplementary Materials for details). The Hamiltonian can be constructed using the basis of the two doublets, p_1 , p_2 , d_1 and d_2 [Fig. 2d]. The combination of these states, $|p_\pm\rangle = \frac{1}{\sqrt{2}}(|p_1\rangle \pm i|p_2\rangle)$ and $|d_\pm\rangle = \frac{1}{\sqrt{2}}(|d_1\rangle \pm i|d_2\rangle)$, carry finite total angular momenta (TAM) that are opposite for the $+$ and $-$ states (see Supplementary Materials). Emulating fermionic spin and orbit with the TAM and parity, respectively, we find the following photonic Hamiltonian for a DP,

$$\hat{\mathcal{H}} = \omega_0 + v \begin{pmatrix} (\eta + 1)q_z \hat{1} & \hat{\mathcal{A}} \\ \hat{\mathcal{A}}^\dagger & (\eta - 1)q_z \hat{1} \end{pmatrix} + \mathcal{O}(q^2), \quad \hat{\mathcal{A}} \equiv g_0 \hat{1} + \vec{g} \cdot \hat{\vec{\sigma}}. \quad (4)$$

where ω_0 is the frequency of the DP, v is the characteristic group velocity. $\hat{1}$ is the 2×2 identity matrix, $\hat{\vec{\sigma}}$ is the Pauli matrix vector. The dimensionless $\vec{k} \cdot \vec{P}$ parameter η here plays an role to distinguish the type-I ($|\eta| < 1$) and type-II ($|\eta| > 1$) DPs. $g_0 = i\alpha q_y$, $g_x = -i\alpha q_x$,

$g_y = i\beta q_x$, $g_z = -\beta q_y$ with $\vec{q} \equiv \vec{k} - (\pi, \pi, k_0)$, where α and β are the (real) $\vec{k} \cdot \vec{P}$ coefficients, and $\mathcal{O}(q^2)$ denotes the higher-order quadratic warping terms. Here the spin-orbit coupling is emulated by the k -linear interaction between the p and d bands due to quasi-conservation of the TAM [29]. The 3D Dirac wave can be regarded as a series of q_z -dependent 2D Dirac waves of which the Dirac mass, $m_D \equiv vq_z$, can be positive, negative, or zero [29, 42].

Derived type-II and type-I Weyl Points

A DP can be regarded as composed of a pair of WPs of opposite Chern numbers. Thus when the space symmetry is reduced WPs can emerge from DPs [29]. To realize the WPs, we deform the unit-cell structure in such a way (as displayed in Fig. 3a) that the two screw symmetries S_x and S_y , the three mirror symmetries $M_1 := (x, y) \rightarrow (y, x)$, $M_2 := (x, y) \rightarrow (-y, -x)$, and $M_z := z \rightarrow -z$, as well as the inversion symmetry \mathcal{P} are broken. However, the C_2 symmetry is preserved. The removal of the two screw symmetries lifts the double degeneracy on the MA line. However, accidental degeneracy between bands of opposite parity is protected by the C_2 symmetry. The chiral structure of the PhC results in p_{\pm} - and d_{\pm} -like states in the photonic bands. The crossings between the p and d bands results in WPs of Chern number ± 1 (see Supplementary Materials for a $\vec{k} \cdot \vec{P}$ analysis). We identify six WPs in Fig. 3b (there are more WPs at higher frequency, explaining the nonzero total Chern number). Fig. 3b also shows that there are four type-II WPs and two type-I WPs. The 3D dispersions of both type-I and type-II WPs on the lowest d -band are shown in Fig. 3c. Our PhC architecture thus allows realization of type-II WPs using dissipationless all-dielectric materials.

Robust surface states

According to the bulk-edge correspondence principle [2–4], the (100) surface states of the tetragonal PhC can reveal the Z_2 topology of the DPs. We then calculate the surface and projected bulk photonic spectrum using a supercell stacking along the x direction [see Methods]. Fig. 4a shows a gapless surface band traversing the projected photonic band gap. This surface band is between the upper and lower branches of the type-I DP, but above both branches of the type-II DP. Thus the gapless surface band is induced by the type-I topological DPs. Nonetheless, both type-I and type-II DPs have the same Z_2 topology (see Fig. 2d). The topological surface states carry finite TAM as indicated in Fig. 4b by the

winding profile of the Poynting vectors. The sign of the photonic TAM is changed when the wavevector is reversed (see Fig. 4b). This property is similar to the “spin-wavevector locking” on the edges of topological insulators [2, 3]. We find that the two symmetries, S_y and \mathcal{T} , guarantee that the spectrum in the surface BZ is symmetric under the transformation $(k_y, k_z) \rightarrow (\pm k_y, \pm k_z)$ (see Methods). It was recently discovered that the surface states of the topological DPs form a double-helicoid surface states with such spectral symmetry. The non-chiral surface bands of our PhC, are distinctive from the chiral surface states due to WPs [25, 27, 28]. Moreover, the topological surface states here are below the light-line and hence form cavity states on the PhC-air interfaces with no need for additional cladding.

The robustness of the topological surface states can be revealed via their frequency stability against surface modifications. Fig. 4c shows that the frequency of the topological surface state is quite robust and insensitive to variations of the thickness of a dielectric slab placed on top of the PhC surface. The change of frequency is within 2.5%, although the field profile has been substantially modified (see Fig. 4d). In contrast, the frequency of a conventional PhC cavity state with woodpile-PhC cladding is much more sensitive to the thickness of the slab [43] (see inset of Fig. 4c and details in Methods), despite the fact that the woodpile PhC has a large complete photonic band gap of $\delta\omega/\omega = 21\%$ while our PhC has no complete photonic band gap. The topological surface states thus form resilient, subwavelength quasi-2D photonic systems. The nontrivial topology/Berry-phases and the gapless spectrum distinct them from normal PhC surface states [44, 45].

Spectral and optical properties

Both type-I and type-II DPs appear in Fig. 2. A more careful study is presented in Fig. 5. From Eq. (4), the spectrum of the DPs in the k_x - k_z plane (Fig. 5a) is

$$\omega = \omega_0 + v\eta q_z + v\tau\sqrt{q_z^2 + \gamma^2 q_x^2}, \quad (5)$$

where $\tau = \pm$ stands for the upper and lower branches of the DP, respectively, the dimensionless parameters $\gamma = \sqrt{\alpha^2 + \beta^2}$ and η measure the deformation of the Dirac cone. Particularly, $|\eta| > 1$ for type-II DPs, whereas $|\eta| < 1$ for type-I DPs. The isofrequency contour near a type-II DP is a hyperbolic curve (Fig. 5b). In contrast, the isofrequency contours near a type-I DP is of elliptical shapes. For a type-II DP, when $\omega = \omega_0$, the two branches touch each other and the isofrequency contour becomes a pair of crossing lines (Fig. 5c),

between which the angle is $\theta_{DP} = 2 \arctan \left(\sqrt{\frac{\eta^2 - 1}{\gamma^2}} \right)$. This quantity sets the bounds on the refraction angles near a type-II DP as $\pm \frac{1}{2}(\pi - \theta_{DP})$.

The dispersion of the type-II DP in the k_x - k_y plane is distinctive from the existing type-I DPs [29, 31, 32] (see Fig. 5d). This spectrum can be understood via the $\vec{k} \cdot \vec{P}$ Hamiltonian (4) which yields $\omega_{\tau,i}(\vec{q}) = \omega_0 + v\eta q_z + v\tau \sqrt{q_z^2 + \gamma^2 |q_i|^2} + \mathcal{O}(q^2)$ for $i = 1, 2$, with $\tau = \pm$ and $q_1 = q_x + q_y$ and $q_2 = q_y - q_x$. This spectrum is nondegenerate for finite q_x and q_y . The two-fold degeneracy is restored only when $q_x = 0$ or $q_y = 0$, in accordance with the screw symmetries. The ‘‘V-shaped’’ dispersion in Fig. 5d gives elliptical-shaped isofrequency contours or non-closing contours in the k_x - k_y plane (see Figs. 5e and 4f), depending on the quadratic warping terms.

From the unique spectral properties of the type-II DPs, using frequency and wavevector matching, we derive the anomalous refraction of light: there are two concurrent refraction beams of opposite angles (see schematic in Fig. 5g). An analytic proof is detailed in the Methods section, which is confirmed by the model calculation in Figs. 5h and 5i for various frequencies, incident angles, and parameters. Interestingly, we find that there is no refraction for $\eta > 1$, whereas for $\eta < -1$ there are two refraction beams of opposite refraction angles. Since the two DPs at opposite wavevectors have opposite η , the above property can be exploited for *selective excitation* of type-II DPs. Away from the $k_x = \pi$ and $k_y = \pi$ planes, the photonic spectrum is nondegenerate, leading to two pairs of beams with opposite refraction angles, as shown in Fig. 5i by varying the angle of incidence $\phi_i = \text{Arg}(q_x + iq_y)$. Zero refraction angle is realized when ϕ_i is close to $\frac{\pi}{4}$, $\frac{3\pi}{4}$, $\frac{5\pi}{4}$, or $\frac{7\pi}{4}$, due to vanishing group velocity in the k_x - k_y plane.

The above unconventional optical properties also holds for type-II WPs. Since WPs are two-fold degenerate, there can only be one pair of refraction beams. Concurrent positive and negative refraction was found and confirmed by time-domain simulation in a 2D photonic system before [46]. Here we find, from frequency-wavevector conservation, that concurrent negative and positive refraction can also be realized in 3D all-dielectric PhCs through type-II DPs/WPs. A time-domain simulation is demanded to further investigate the anomalous refraction, which, however, is beyond the scope of this work.

Discussion

The band topology induced by crystalline symmetries are in the context of topological crystalline states [47, 48]. Weak disorders that preserve the crystalline symmetry on average should preserve the DPs and their topological surface states [29, 48]. The topological surface states here can exist on the PhC-air interface without further cladding, even though such interface does not preserve the screw symmetries. The robustness of the surface photonic bands show superiority over conventional PhC cavity states. This suggests that topology can be a possible tool to suppress inhomogeneous broadening which is a main obstacle for scalable optical and quantum devices. Our all-dielectric topological PhC architecture may inspire future discovery of other 3D topological photonic states in all-dielectric photonics, and stimulate future synergy between subwavelength photonic topological materials and optoelectronics on PhC surfaces.

Note added: When this paper was under review for the final round, a proposal of type-II DPs in electronic materials with robust Fermi arcs, has appeared [49].

Methods

Symmetry transformation of photonic states

A photonic state $\Psi_{n\vec{k}}(\vec{r})$ transforms under the $\Theta_x = S_x * \mathcal{T}$ operation as follows,

$$\Theta_x \Psi_{n\vec{k}}(\vec{r}) = \hat{M}_y \hat{M}_z \hat{t}_h \Psi_{n\vec{k}}^*(S_x \vec{r}), \quad (6)$$

where \hat{M}_y and \hat{M}_z are the mirror transformation for the electromagnetic fields along the y and z directions, respectively. For instance,

$$\hat{M}_y E_i = \bar{\delta}_{iy} E_i, \quad \hat{M}_z H_i = -\bar{\delta}_{iz} H_i, \quad i = x, y, z, \quad (7)$$

$$\bar{\delta}_{ij} = \begin{cases} 1, & \text{if } i \neq j \\ -1, & \text{if } i = j \end{cases}, \quad (8)$$

and the operator \hat{t}_h reverses the sign of the magnetic field. Acting Θ_x twice yields,

$$\Theta_x^2 \Psi_{n\vec{k}}(\vec{r}) = \Psi_{n\vec{k}}(S_x^2 \vec{r}) = \Psi_{n\vec{k}}(T_{100} \vec{r}) = e^{ik_x} \Psi_{n\vec{k}}(\vec{r}). \quad (9)$$

Refraction

The photonic dispersion in the medium with refraction index n_i is given by $\omega = c|\vec{k}|/n_i$. We consider a light beam injected from a medium with a refraction index $n_i > 1.65$ into the PhC to enable frequency and wavevector matching with the Dirac cones. Around the DP at $\vec{K}_0 = (\pi, \pi, k_0)$, the dispersion in the medium can be expressed as $\omega = c|\vec{k}|/n_i = c|\vec{K}_0 + \vec{q}|/n_i$ where $\vec{q} = \vec{k} - \vec{K}_0$. Since the perpendicular wavevector k_z is not conserved during refraction, we can always set

$$q_x = q_{\parallel} \cos(\phi_i), \quad q_y = q_{\parallel} \sin(\phi_i) \quad (10)$$

for fixed q_{\parallel} , while adjusting k_z to keep a constant frequency. The angle ϕ_i is varied from 0 to 2π . The refraction in the x - z plane is determined by matching the frequency and the parallel wavevector, yielding

$$\omega - \omega_0 = v(\eta q_z + \tau \sqrt{q_z^2 + \gamma^2 q_x^2}), \quad \tau = \pm 1. \quad (11)$$

The perpendicular wavevector q_z in the PhC is determined by the above equation, which has two solutions for $\eta < -1$

$$q_z^{\tau} = \frac{\eta(\omega - \omega_0) + \tau \sqrt{(\omega - \omega_0)^2 + v^2(\eta^2 - 1)\gamma^2 q_x^2}}{v(\eta^2 - 1)}. \quad (12)$$

The refraction angle is determined through the group velocities in the PhC as, $\theta_r \equiv -\arctan(\frac{v_x}{v_z})$. Using the dispersion in Eq. (5), we find that $v_z = v \left(\eta + \frac{\tau q_z}{\sqrt{\gamma^2 q_x^2 + q_z^2}} \right)$, $v_x = \frac{\tau v \gamma q_x}{\sqrt{\gamma^2 q_x^2 + q_z^2}}$. Inserting Eq. (12) into the definition of the refraction angle, we obtain

$$\theta_{r2} = -\theta_{r1} = -\arctan \left(\frac{v \gamma q_x}{\sqrt{(\omega - \omega_0)^2 + v^2(\eta^2 - 1)\gamma^2 q_x^2}} \right). \quad (13)$$

Refraction for generic \vec{q} (i.e., away from the x - z or y - z plane) is given in details in the Supplementary Materials.

Calculation of surface states

The surface states are obtained by supercell calculations. The supercell is periodic in the y - z plane but finite in the x direction. There are seven layers of unit cell along this direction as sandwiched by air layers of length $3a$ on the left and right, separately. The simple cladding

medium (air) used here is non-topological for all polarizations and useful to study topological surface states below the light-line. The supercell structure is set to preserve the S_y symmetry. Since S_y transforms (k_y, k_z) to $(k_y, -k_z)$ in the surface BZ, the surface spectrum is symmetric with respect to $k_z = 0$ and $k_z = \pi$. In addition, the \mathcal{T} symmetry guarantees that the surface spectrum is invariant under the transformation (k_y, k_z) to $(-k_y, -k_z)$. Therefore the surface photonic dispersion is also symmetric with respect to $k_y = 0$ and $k_y = \pi$. As detailed in Ref. [50], although there are other topological degeneracies in our PhC (such as nodal lines), they do not affect the surface states on the (100) and (010) surfaces.

In the calculation of the reference slab-defect states, we have set the permittivity of the slab-defect layer as $\varepsilon = 8$ (the same as that of the dielectric slab on top of the topological PhC). The logs of the woodpile PhCs above and below the slab-defect layer are of width $0.25a$, height $0.3a$ and permittivity of 12 (silicon).

Acknowledgements

We thank Sajeev John, Zhengyou Liu, Ling Lu, Chen Fang, Huanyang Chen, Yun Lai, Chunying Qiu, and Jie Luo for many inspiring discussions.

Competing interests

The authors declare no competing financial interests.

Contributions

J.H.J conceived the idea and wrote the manuscript. J.H.J and Z.H.H designed the photonic architecture. H.X.W, Y.C, H.Y.K and J.H.J did the theoretical analysis and calculations. J.H.J guided the research.

Funding

H.X.W and J.H.J acknowledge supports from the National Science Foundation of China (Grant no. 11675116) and the Soochow university. Z.H.H is supported by National Science Foundation of China (Grant no. 11574226). Y.C and H.Y.K are supported by NSERC of Canada and Center for Quantum Materials at the University of Toronto.

Data availability

All relevant data are available from the corresponding author J.H.J (email: jianhua-jiang@suda.edu.cn or joejhjiang@hotmail.com).

References

- [1] Dirac, P. A. M. The quantum theory of the electron. *Proc. Roy. Soc. A* (London) **117**, 610-624. (1928).
- [2] Hasan, M. Z. & Kane, C. L. Topological insulators. *Rev. Mod. Phys.* **82**, 3045-3067 (2010).
- [3] Qi, X.-L. & Zhang, S.-C. Topological insulators and superconductors. *Rev. Mod. Phys.* **83**, 1057-1110 (2011).
- [4] Vafek, O. & Vishwanath, A. Dirac fermions in solids: from high- T_c cuprates and graphene to topological insulators and Weyl semimetals. *Ann. Rev. Cond. Matt. Phys.* **5**, 83-112 (2014).
- [5] Haldane, F. D. M. & Raghu, S. Possible realization of directional optical waveguides in photonic crystals with broken time-reversal symmetry. *Phys. Rev. Lett.* **100**, 013904 (2008).
- [6] Lu, L., Joannopoulos, J. D. & Soljačić, M. Topological photonics. *Nat. Photon.* **8**, 821-829 (2014).
- [7] Yang, Z., Gao, F., Shi, X., Lin, X., Gao, Z., Chong, Y. & Zhang, B. Topological acoustics. *Phys. Rev. Lett.* **114**, 114301 (2015).
- [8] Xiao, M., Chen, W.-J., He, W.-Y. & Chan, C. T. Synthetic gauge flux and Weyl points in acoustic systems. *Nat. Phys.* **11**, 920-924 (2015).
- [9] He, C., Ni, X., Ge, H., Sun, X.-C., Chen, Y.-B., Lu, M.-H., Liu, X.-P. & Chen, Y.-F. Acoustic topological insulator and robust one-way sound transport. *Nat. Phys.* **12**, 1124-1129 (2016).
- [10] Süsstrunk, R. & Huber, S. D. Observation of phononic helical edge states in a mechanical topological insulator. *Science* **349**, 47-50 (2015).
- [11] Rocklin, D. Z., Chen, B. G.-g., Falk, M., Vitelli, V. & Lubensky, T. C. Mechanical Weyl modes in topological Maxwell lattices. *Phys. Rev. Lett.* **116**, 135503 (2016).
- [12] Zhang, X. Observing Zitterbewegung for photons near the Dirac point of a two-dimensional photonic crystal. *Phys. Rev. Lett.* **100**, 113903 (2008).
- [13] Huang, X. Q., Lai, Y., Hang, Z. H., Zheng, H. H. & Chan, C. T. Dirac cones induced by

- accidental degeneracy in photonic crystals and zero-refractive-index materials. *Nat. Mater.* **10**, 582-586 (2011).
- [14] Rechtsman, M. C., Zeuner, J. M., Tünnermann, A., Nolte, S., Segev, M. & Szameit, A. Strain-induced pseudomagnetic field and photonic Landau levels in dielectric structures. *Nat. Photon.* **7**, 153-158 (2013).
- [15] Khanikaev, A. B., Mousavi, S. H., Tse, W.-K., Kargarian, M., MacDonald, A. H. & Shvets, G. Photonic topological insulators. *Nat. Mater.* **12**, 233-239 (2013).
- [16] Chen, W.-J., Jiang, S.-J., Chen, X.-D., Dong, J.-W., & Chan, C. T. Experimental realization of photonic topological insulator in a uniaxial metacrystal waveguide. *Nat. Commun.* **5**, 5782 (2014).
- [17] Ma, T., Khanikaev, A. B., Mousavi, S. H. & Shvets, G. Guiding electromagnetic waves around sharp corners: topologically protected photonic transport in metawaveguides. *Phys. Rev. Lett.* **114**, 127401 (2015).
- [18] Wu, L.-H. & Hu, X. Scheme for achieving a topological photonic crystal by using dielectric material. *Phys. Rev. Lett.* **114**, 223901 (2015).
- [19] Xu, L., Wang, H.-X., Xu, Y.D., Chen, H.Y. & Jiang, J.-H., Accidental degeneracy in photonic bands and topological phase transitions in two-dimensional core-shell dielectric photonic crystals. *Opt. Express* **24**, 18059-18071 (2016).
- [20] Wang, Z., Chong, Y., Joannopoulos, J. D. & Soljačić, M. Observation of unidirectional backscattering-immune topological electromagnetic states. *Nature* (London) **461**, 772-775 (2009).
- [21] Poo, Y., Wu, R.-X., Lin, Z., Yang, Y. & Chan, C. T. Experimental Realization of Self-Guiding Unidirectional Electromagnetic Edge States. *Phys. Rev. Lett.* **106**, 093903 (2011).
- [22] Hafezi, M., Mittal, S., Fan, J., Migdall, A. & Taylor, J. Imaging topological edge states in silicon photonics. *Nat. Photon.* **7**, 1001-1005 (2013).
- [23] Rechtsman, M. C., Zeuner, J. M., Plotnik, Y., Lumer, Y., Podolsky, D., Dreisow, F., Nolte, S., Segev, M. & Szameit, A. Photonic Floquet topological insulators. *Nature* (London) **496**, 196-200 (2013).
- [24] Mittal, S., Ganeshan, S., Fan, J., Vaezi, A. & Hafezi, M. Measurement of topological invariants in a 2D photonic system. *Nat. Photon.* **10**, 180-183 (2016).
- [25] Lu, L., Fu, L., Joannopoulos, J. D. & Soljačić, M. Weyl points and line nodes in gyroid

- photonic crystals. *Nat. Photon.* **7**, 294-299 (2013).
- [26] Lu, L., Wang, Z., Ye, D., Ran, L., Fu, L., Joannopoulos, J. D. & Soljačić, M. Experimental observation of Weyl points. *Science* **349**, 622-624 (2015).
- [27] Gao, W., Yang, B., Lawrence, M., Fang, F., Béri, B. & Zhang, S. Plasmon Weyl degeneracies in magnetized plasma. *Nat. Comm.* **7**, 12435 (2016).
- [28] Chen, W.-J., Xiao, M. & Chan, C. T. Experimental observation of robust surface states on photonic crystals possessing single and double Weyl points. *Nat. Commun.* **7**, 13038 (2016).
- [29] Wang, H.-X., Xu, L., Chen, H.Y. & Jiang, J.-H. Three-dimensional photonic Dirac points stabilized by point group symmetry. *Phys. Rev. B* **93**, 235155 (2016).
- [30] Xiao, M., Lin, Q. & Fan, S. Hyperbolic Weyl point in reciprocal chiral metamaterials. *Phys. Rev. Lett.* **117**, 057401 (2016).
- [31] Lu, L., Fang, C., Fu, L., Johnson, S. G., Joannopoulos, J. D. & Soljačić, M. Symmetry-protected topological photonic crystal in three dimensions. *Nat. Phys.* **12**, 337-340 (2016).
- [32] Slobozhanyuk, A., Mousavi, S. H., Ni, X., Smirnova, D., Kivshar, Y. S. & Khanikaev, A. B. Three-dimensional all-dielectric photonic topological insulator. *Nat. Photon.* **11**, 130-136 (2017).
- [33] Fu, L. & Kane, C. L. Topological insulators with inversion symmetry. *Phys. Rev. B* **76**, 045302 (2007).
- [34] Soluyanov, A. A., Gresch, D., Wang, Z., Wu, Q., Troyer, M., Dai, X. & Bernevig, B. A. Type-II Weyl semimetals. *Nature (London)* **527**, 495-498 (2015).
- [35] Xu, Y., Zhang, F. & Zhang, C. Structured Weyl points in spin-orbit coupled fermionic superfluids. *Phys. Rev. Lett.* **115**, 265304 (2015).
- [36] König, A. & Mermin, N. D. Electronic level degeneracy in nonsymmorphic periodic or aperiodic crystals. *Phys. Rev. B* **56**, 13607-13610 (1997).
- [37] Parameswaran, S. A., Turner, A. M., Arovas, D. P. & Vishwanath, A. Topological order and absence of band insulators at integer filling in non-symmorphic crystals. *Nat. Phys.* **9**, 299-303 (2013).
- [38] Lee, J.-H., Leung, W., Ahn, J., Lee, T., Park, I.-S., Constant, K. & Ho, K.-M. *Layer-by-layer photonic crystal fabricated by low-temperature atomic layer deposition.* *Appl. Phys. Lett.* **90**, 151101 (2007).
- [39] Deubel, M., von Freymann, G., Wegener, M., Pereira, S., Busch, K. & Soukoulis, C. M.

- Direct laser writing of three-dimensional photonic-crystal templates for telecommunications. *Nat. Mater.* **3**, 444-447 (2004).
- [40] <http://ab-initio.mit.edu/wiki/index.php/MITPhotonicBands>.
- [41] Yang, B.-J., Morimoto, T. & Furusaki, A. Topological charges of three-dimensional Dirac semimetals with rotation symmetry. *Phys. Rev. B* **92**, 165120 (2015).
- [42] Morimoto, T. & Furusaki, A. Weyl and Dirac semimetals with Z_2 topological charge. *Phys. Rev. B* **89**, 235127 (2014).
- [43] John, S. & Yang, S. Electromagnetically Induced Exciton Mobility in a Photonic Band Gap. *Phys. Rev. Lett.* **99**, 046801 (2007).
- [44] Ishizaki, K. & Noda, S. Manipulation of photons at the surface of three-dimensional photonic crystals. *Nature* (London) **460**, 367-370 (2009).
- [45] Joannopoulos, J. D., Johnson, S. G., Winn, J. N. & Meade, R. D. *Photonic Crystals: Molding the Flow of Light*. (Princeton University Press, 2008).
- [46] Luo, J., Xu, P., Sun, T. & Gao, L. Tunable beam splitting and negative refraction in heterostructure with metamaterial. *Appl. Phys. A* **104**, 1137-1142 (2011).
- [47] Fu, L. Topological crystalline insulators. *Phys. Rev. Lett.* **106**, 106802 (2011).
- [48] Fu, L. & Kane, C. L. Topology, delocalization via average symmetry and the symplectic Anderson transition. *Phys. Rev. Lett.* **109**, 246605 (2012).
- [49] Chang, T.-R. *et al.* Type-II symmetry-protected topological Dirac semimetals. *Phys. Rev. Lett.* **119**, 026404 (2017).
- [50] Wang, H.-X., Chen, Y., Hang, Z. H., Kee, H.-Y. & Jiang, J.-H. 3D Z_2 Topological Nodes in Nonsymmorphic Photonic Crystals: Ultrastrong Coupling and Anomalous Refraction. Preprint at <https://arxiv.org/abs/1608.02437>.

Figure Legends

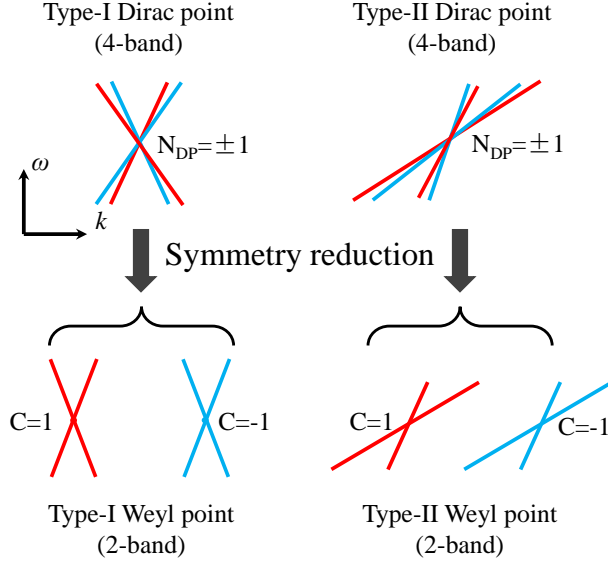


FIG. 1. **Type-I and type-II Dirac/Weyl points.** A type-I Dirac point (4-band degeneracy point), characterized by a topological number $N_{DP} = \pm 1$, consists of two type-I Weyl points (2-band degeneracy points) with opposite Chern number, $C = \pm 1$. A type-II Dirac point consists of two type-II Weyl points with Chern number $C = \pm 1$. A type-I Dirac (Weyl) point has four (two) branches, among which there are both positive and negative group velocities. In a type-II Dirac/Weyl point, instead, there are only branches of positive (or negative, not shown in the figure) group velocities. The definition of the topological charge of the Dirac points N_{DP} are given in the main text.

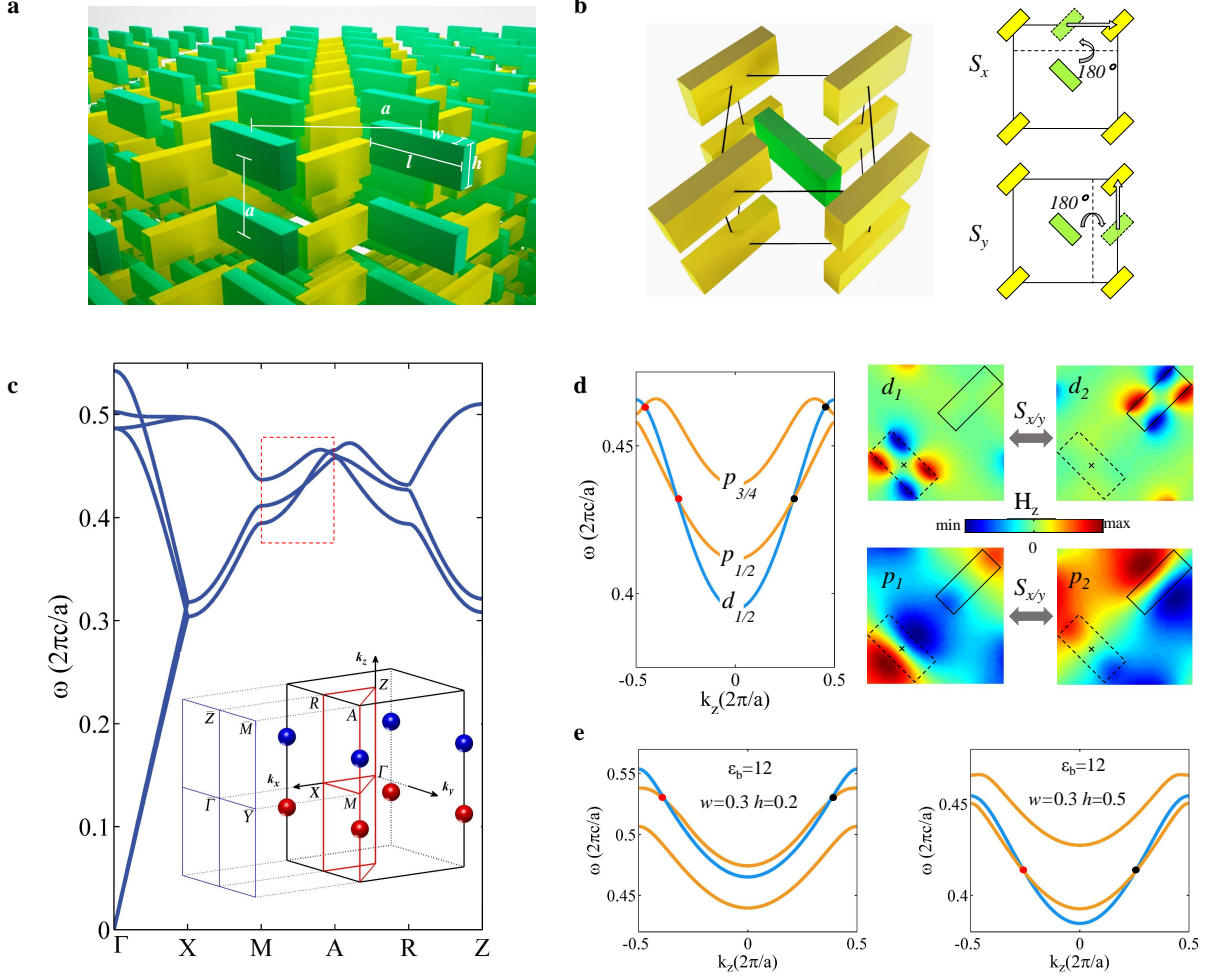


FIG. 2. **All-dielectric photonic-crystals for Dirac points.** **a**, 3D view of the PhC. The yellow and green blocks are of the same material and shape and permittivity ϵ_b . The background is polymer $\epsilon_m = 1.9$. **b**, Left: 3D structure of a unit cell (boundaries are indicated by black lines). The lattice constant along all directions is a . Right: Illustration of the two orthogonal screw symmetries S_x and S_y in top-down view. **c**, Photonic band structure for $\epsilon_b = 16$, $l = 0.5a$, $w = 0.2a$, and $h = 0.5a$. Inset: bulk and surface BZs. The $k_x = \pi$ plane is doubly degenerate due to the screw symmetry. **d**, Left: Parity inversion on the MA line (each curve represents a doublet). Right: magnetic field profiles of the p - and d -wave doublets, $p_{1/2}$ and $d_{1/2}$, respectively. The doubly degenerate states are connected by the screw symmetries. **e**, Band inversion for other substantially different parameters. DPs of topological charge $N_{DP} = +1, -1$ are labeled as red and blue (red and black) in **c** (**e**), separately. Frequencies are in unit of $2\pi c/a$ with c being the speed of light in vacuum.

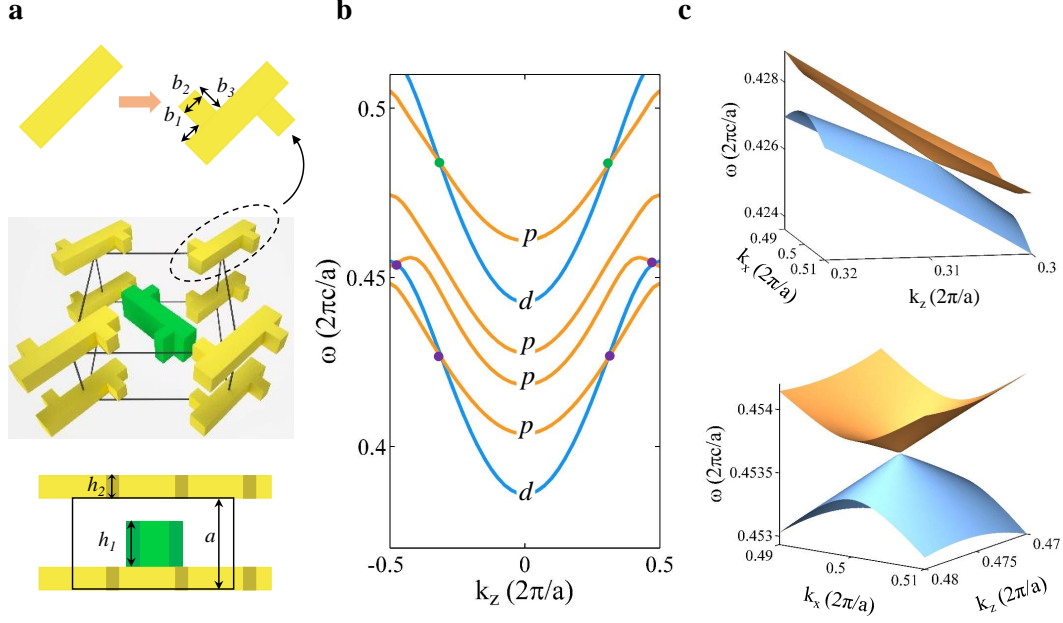


FIG. 3. **Weyl points derived from Dirac points.** **a**, Unit-cell structure of the symmetry-broken PhC. Upper panel: 3D view with zoom-in illustration of structure deformations. Lower panel: side view from $[1\bar{1}0]$ direction. The geometry parameters are $b_1 = 0.1$, $b_2 = 0.11$, $b_3 = 0.094$, $h_1 = 0.5$, and $h_2 = 0.3$. The z coordinates of the centers of the two types of dielectric blocks are 0 and $0.65a$, respectively. **b**, Band structure on the MA line for part of the first six photonic bands indicates removal of double degeneracy and linear-crossing between non-degenerate p - and d -states. These crossings are identified as type-I and type-II WPs. Purple (green) dots stand for WPs with Chern number -1 (+1). **c**, Dispersions of a type-II WP (upper panel) and a type-I WP (lower panel). The former is due to the crossing between band 1 and 2, while the latter originates from the crossing between band 1 and 3. The bands are numerated in ascending order at the M point.

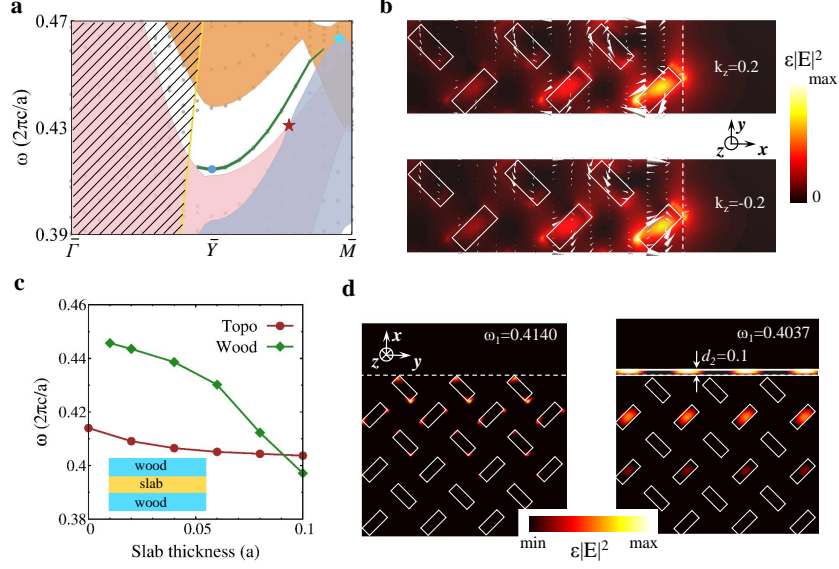


FIG. 4. **Dirac points and topological surface states.** **a**, Surface band and projected bulk bands on (100) PhC-air interface. The blue (brown) star represents a type-I (type-II) DP, which are the crossing point of band 1,2 (gray region) and band 5,6 (brown region) [band 3,4 (pink region)]. The surface band (green curve) is below the light-line (the golden line). The region above the light-line is depicted by the shadow. Gray dots represent the spectrum from a finite-size supercell calculation (see Methods). **b**, Energy density and Poynting vector profiles for the topological surface states at two opposite wavevectors with $k_y = \pi$. **c**, Stability of the topological (“Topo”) surface states. Frequency of the topological surface state at \bar{Y} vs. thickness of a slab with permittivity $\epsilon = 8$ on top of the PhC surface. The reference curve is the same dependence for the slab-defect state induced by a slab of the same permittivity embedded in a woodpile (“Wood”) PhC (structure schematically shown in the inset). **d**, Field energy distribution of the topological surface states at \bar{Y} point for slab thickness 0 (Left) and $0.1a$ (Right), respectively.

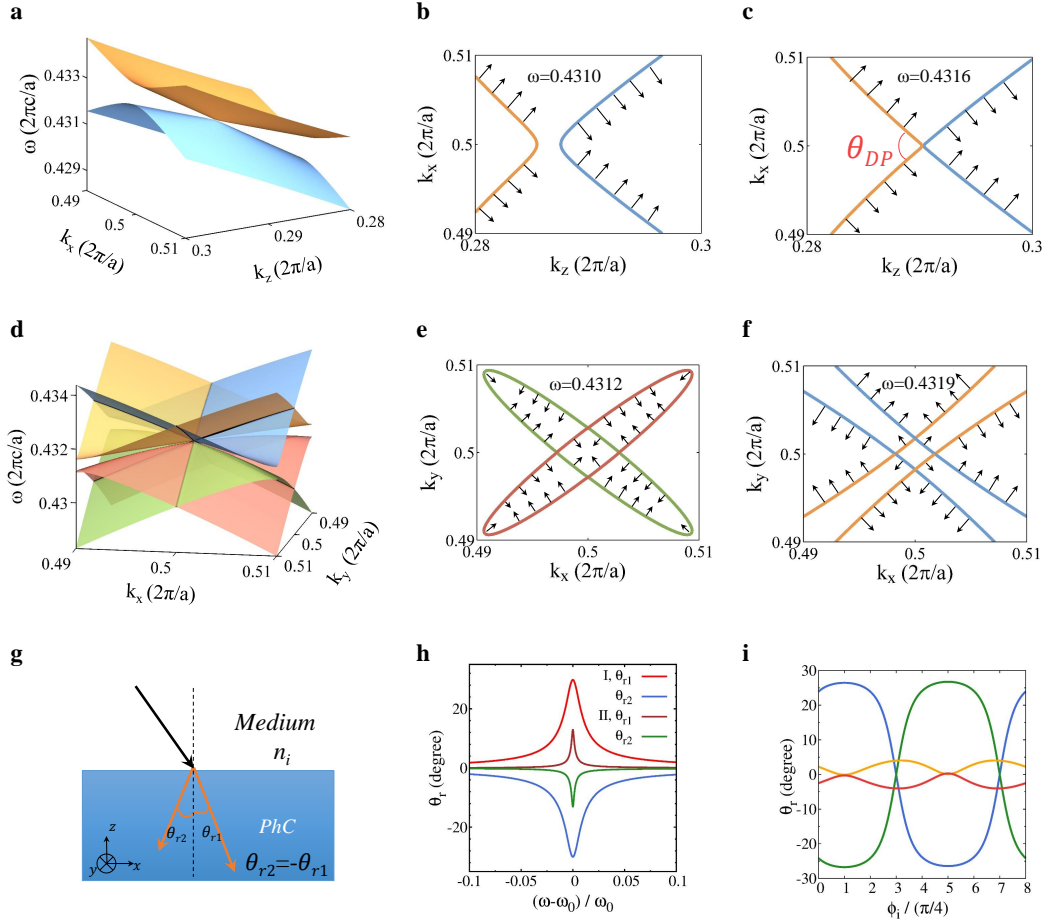


FIG. 5. **Type-II Dirac cone and anomalous refraction.** **a**, Type-II Dirac dispersion on the k_x - k_z plane. **b**, Isofrequency contours (orange and blue curves for the upper and lower branches, respectively) and group velocities (black arrows) on the k_x - k_z plane for a frequency below the type-II DP. **c**, Similar to **b**, but for the frequency at the DP. **d**, Dispersion of the Dirac cone on the k_x - k_y plane. **e** and **f**, Isofrequency contours on the k_x - k_y plane for frequencies below and above the DP, respectively. **g**, Schematic of anomalous refraction of type-II DPs: concurrent positive and negative refraction with opposite angles. **h**, Refraction angles vs. frequency for two cases with $\phi_i = 0$. Case I: $\gamma = 1$ and $q_{\parallel} = 0.2\frac{\pi}{a}$. Case II: $\gamma = 0.4$ and $q_{\parallel} = 0.1\frac{\pi}{a}$. **i**, Refraction angles vs. angle ϕ_i for $\gamma = 1$ and $q_{\parallel} = 0.1\frac{\pi}{a}$ and $\frac{\delta\omega}{\omega_0} = 0.005$ with $\omega_0 = 0.4\frac{2\pi c}{a}$.